iScience

Article
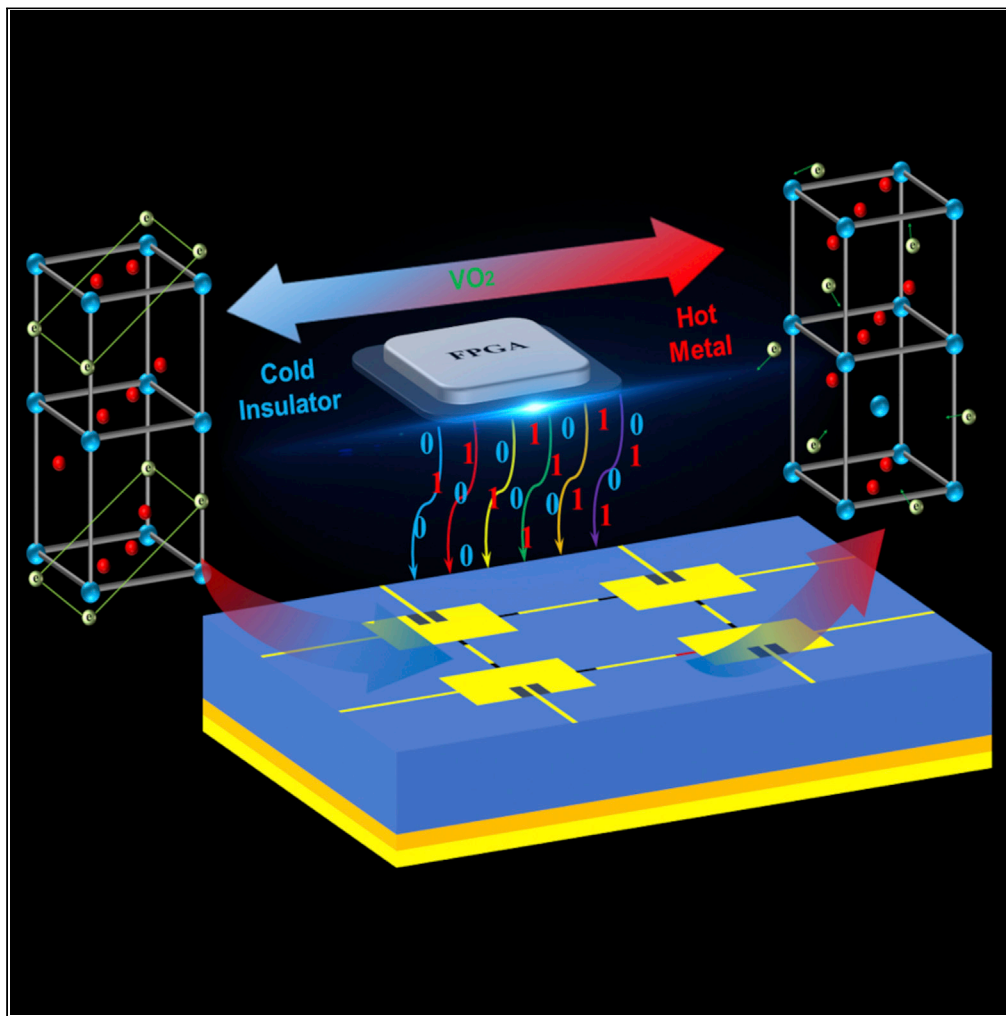
Redefinable planar microwave passive electronics enabled by thermal controlled VO$_2$/Cu hybrid matrix

Lei Sang, Zhikun Zhou, Ji Xu, ..., Tao Yuan, Yongfeng Mei, Wen Huang

huangw@hfut.edu.cn

Highlights

A thermal-controlled EM functionally reconfigurable array device is demonstrated

Microwave device can switch between antenna array and cascaded filter functions

Hybrid EM functions such as cascaded antenna arrays and filters are enabled

By varying in time the phase of the VO$_2$ units, number of passive devices can be reduced

Article

Redefinable planar microwave passive electronics enabled by thermal controlled VO₂/Cu hybrid matrix

Lei Sang,[1] Zhikun Zhou,[1] Ji Xu,[1] Xing Li,[2] Wei He,[4] Hong Yang,[5] Xiaochen Chen,[4] Tao Yuan,[3] Yongfeng Mei,[2] and Wen Huang[1,6,*]

SUMMARY

A planar microwave array device with complex electromagnetic functional reconfigurability is demonstrated by means of phase transition film VO₂ to manipulate the electromagnetic distribution. Based on planar patch architecture, the microwave device can switch between antenna array and cascaded filter functions. Furthermore, hybrid EM functions such as cascaded antenna arrays and filters are enabled, themselves with further reconfigurability. Therefore, a single design realizes many mono and hybrid antenna and filter functions, which are determined by the order of the array. For simplicity of demonstration, a 2 × 2 array device working at three reconfigurable center frequency points of 3.1, 3.7, and 4.4 GHz, fully compatible with standard planar CMOS processing. A comprehensive design method is proposed to meet the design requirements of a patch-based antenna array and cascaded filter. Based on the functionally reconfigurable microwave device, the front-end circuit could be recombined to suitable for multifunctional microwave systems.

INTRODUCTION

In recent years, with the rapid development of multi-network integration (Li et al., 2021), multi-purpose wireless terminals (Sui and Wu, 2018), and multifunctional sensing functions (Cai et al., 2021), multifunctional circuits are beginning to demonstrate value in reducing the cost and complexity of electronic systems (Cheng et al., 2018; Sim et al., 2019). High integration is one of the development trends of devices (Huang et al., 2018; Sang et al., 2019; Huang et al., 2020; Luo et al., 2021). Functionally reconfigurable devices and circuits are designed to switch between individual functions according to the immediate demand of the application, supporting use by customers seeking a single component to fulfill a diverse range of roles across a diverse application space (Pan et al., 2020; Zhang et al., 2022). Functional reconfigurability extends beyond mere tunability, as the basic mode of operation of a functionally reconfigurable device can switch between modes with characteristically different behavior, and the available modes of operation can be configured for use individually or concurrently. Conventional microwave links and systems consist of stand-alone microwave devices. The functions of these conventional microwave devices are immutable, meaning that an existing microwave link cannot be significantly modified to meet a different application scenario. According to the dynamic application requirements presented to a system, the microwave link was refactored by adjusting the function of the microwave device. This principle both greatly increases the reusability of the microwave system, and reduces the quantity of separate systems required as one FRMAD can substitute many others. This aspect reduces both the fixed infrastructure and recurring operational maintenance costs of an implemented microwave system. In addition to reducing development costs via a flexible platform, functionally reconfigurable circuits also reduce the development time of a given electronic system by reducing the number of discrete components requiring qualification prior to end-use.

Reconfigurability of digital circuitry is presently realized with field-programmable gate arrays (FPGA) in a general and scalable form. Similarly, functionally reconfigurable microwave passive devices can generally exhibit behavior resembling, either alone or jointly, a reconfigurable antenna, a reconfigurable filter, or a reconfigurable splitter. However, replicating reconfigurability in the sense of an FPGA is difficult in the microwave frequency domain because in addition to guiding the steady state flow of a signal like an FPGA, the time-varying electromagnetic (EM) field on a high-frequency device needs to be redistributed in space on demand for impedance matching and EM coupling purposes. Current studies of reconfigurable

[1]School of Microelectronics, Hefei University of Technology, Hefei 230601 China

[2]Department of Materials Science, Fudan University, Shanghai 200433, China

[3]College of Electronics and Information Engineering, Shenzhen University, Shenzhen 518060, China

[4]China Academy of Information and Communication Technology, Beijing 100191, China

[5]China Electronics Standardization Institute, Beijing 100191, China

[6]Lead contact

*Correspondence: huangw@hfut.edu.cn

https://doi.org/10.1016/j.isci.2022.105060

microwave passive devices largely focus on the reconfigurability of a specific performance metric, such as frequency reconfigurability (Yang et al., 2020; Sumana et al., 2021; Chen and Chu, 2016), bandwidth reconfigurability (Maragheh et al., 2019; Song et al., 2019), polarization reconfiguration (Anantha et al., 2017; Li et al., 2020), radiation pattern reconfigurability (Prakash et al., 2021; Zainarry et al., 2018; Boukarkar et al., 2018), etc., while functional reconfiguration is seldom reported.

Our recent work took a further step to demonstrate a planar three-in-one(antenna-filter-splitter) functionally reconfigurable microwave device with different design methodology showing more rigorous design flow and better antenna performance. VO_2 phase transition thin film segments were utilized not only for current switching but also for impedance matching (Sang et al., 2020). Before the phase transition, the VO_2 crystal lattice is in the monoclinic crystal phase, characterized by a low electrical conductivity of $\sim 10^3$ S/m (referred to as the "Low" state in this paper). When heated over 68°C, the VO_2 crystal lattice transitions to the tetragonal crystal phase, characterized by a relatively high electrical conductivity of $\sim 10^6$ S/m (referred to as the "High" state in this paper). Transitions between these states can occur over a few dozens of nanoseconds controlled by temperature (Sang et al., 2020). The microwave performance of VO_2 for reconfigurable microwave planar devices was validated in the reference (Sang et al., 2020), along with a single-resonance element made of Cu and VO_2 thin film, called the basic building block (BBB).

The performance capabilities of a functionally reconfigurable microwave device with only one BBB do not reach the limits of or take full advantage of the BBB. By introducing the BBB array, it can be imaged that there will be significant expansion of performance capabilities. Firstly, antenna arrays and higher order filters are naturally realized based on this new device architecture, which enables much more complex functional reconfigurability, such as the tunability of antenna beam scanning and filter metrics, etc. Secondly, hybrid functionality is enabled in one device, meaning that a subset of the array elements is allocated to perform one function while the rest perform another function. Summarized from previous work, comprehensive design is necessary to balance the performance of the filter and antenna functions to obtain the best collective performance. Following, it can be inferred that more complicated design methods need to be studied for array-based microwave devices. With an elaboration of the design method, processing flow, and experimental results, a functionally reconfigurable microwave array device (FRMAD) with the above-mentioned advanced performance was demonstrated in this work.

RESULTS AND DISCUSSION

Electrothermal characteristics of VO_2

The VO_2 phase transition was measured to abruptly occur when the temperature surpassed 68°C (Lee et al., 2018; Wu et al., 2018). The hysteresis loop of the D.C. electrical conductivity of the sputtered VO_2 on the sapphire substrate is measured and summarized in Figure 1A, which shows suddenly phase transition at temperature of 66°C when heating up, and relatively slow phase transition starting from temperature of 80°C to 60°C when cooling down.

The D.C. electrical conductivity obtains over 10^3 magnitudes from 3000 S/m to 3×10^6 S/m. The D.C. electrical conductivity simultaneously increased by over 3 orders of magnitude from $\sim 0.95 \times 10^3$ S/m to $\sim 1.13 \times 10^6$ S/m as shown in Figure 1B. The inserted table shows the measured DC electrical conductivity of the VO_2 thin film and the inserted photograph is an optical image of the microstrip line sample used for the S-parameters testing.

Figures 1C and 1D exhibit the influence of process temperatures and gas flow ratio on the phase transformation properties of VO_2, respectively. VO_2 devices were made for testing at different process temperatures; voltages were applied to both ends of the device heats up VO_2 to produce phase transition. When the process temperature is higher, the change of the conductivity of VO2 is more obvious due to the degree of crystallization will be greatly improved and the flow ratio of argon and oxygen also has a great effect. The specific experimental work can be referred to the supplemental information.

Design method of thermal and electrical properties of VO_2 in reconfigurable microwave array device

With a FRMAD, different microwave functions should be realized in one physical structure, which involves an iterative process of balancing functional compromises to reach a satisfactory design. For the example used in the paper, some design targets of the antenna and the filter are irreconcilable.
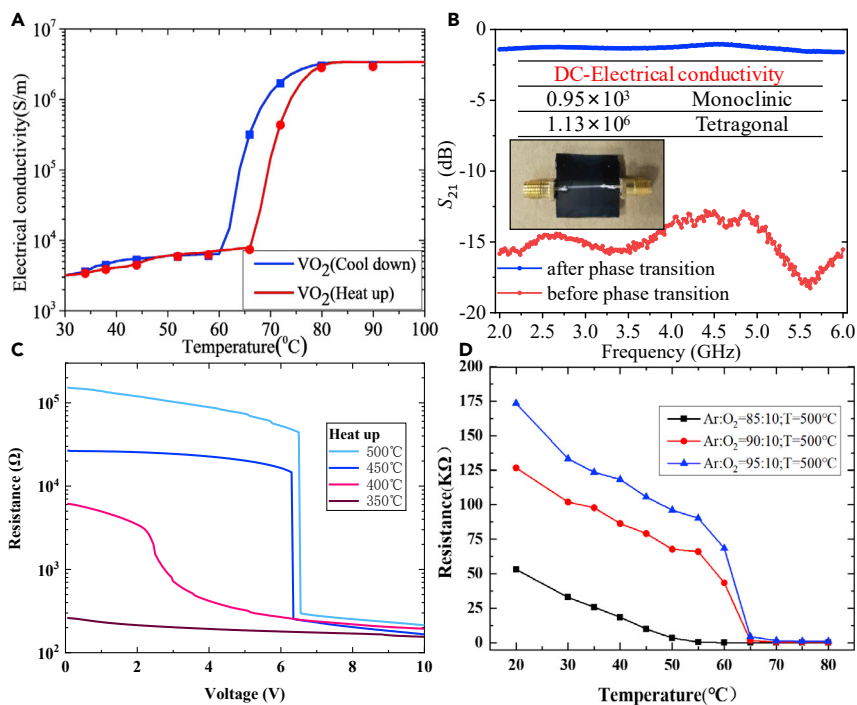
Figure 1. Physical properties of VO₂

(A) The hysteresis loop of the conductivity of VO2 on sapphire substrate with phase changing between the monoclinic phase and tetragonal phase.

(B) A comparison of the transmission loss, S21 (per mm), of the microstrip transmission line using a VO2 thin film before (low conductivity) and after (high conductivity) the phase transition.

(C) The relationship between voltage and resistance at different process temperatures.

(D) The relationship between temperature and resistance at different gas flow ratios.

For both the antenna and filter functions, the alternative operating frequency bands of 5G communication and microwave imaging (MI), 4.4 GHz (5G), 3.7 GHz (5G), and 3.1 GHz (MI), were chosen as the reconfigurable center frequency points. First, the desired performance of each microwave function should be defined and analyzed. The performance metrics should be ranked in the order of importance to the intended application. In this manuscript, the priority ranking of the performance metrics are: the center working frequency point of the antenna, the 1st reconfigurable working frequency point of the filter, the realized gain of the antenna array, the 2nd reconfigurable working frequency point of the filter, and finally the bandwidth of the filter. For antenna array functions, the center frequency point is 4.4 GHz, and the gain is higher than 1.5 dBi. For the filter functions, the center frequency point can be reconfigured to 4.4, 3.7, and 3.1 GHz by using different modes. The insertion loss of the filter is required to be smaller than 3 dB, and the fractional bandwidth (*FBW*) is required to be about 5%.

A 2 × 2 array of BBBs is used to construct the FRMAD, as plotted in Figures 2A and 2B. As seen in Figures 2C–2F, phase transition of VO₂ is controlled by heating power to realize different functional devices through finite element simulation. The simulation results show that the proper heating power is crucial. If the heating power is too small, the VO₂ cannot change into metal state, while if the heating power is too large, heat will diffuse to other switch areas to affect the phase transformation of other switches. Therefore, the appropriate heating power is used to individually control the phase transformation of each switch to achieve a multi-functional device. Optimized initial dimensions for the FRMAD can be obtained by following the design steps. Then, the reconfigurable array device can be modeled in the commercial 3D electromagnetic field analysis software high-frequency structure simulator (HFSS) by Ansys to evaluate each configuration comprehensively. There are two sets of material parameters necessary to describe the properties of the VO₂ thin film corresponding to the phase state before the transition (conductivity: 950 S/m) and the phase state after the transition (conductivity: 1.1×10^6 S/m). The fully optimized dimensions are listed in Figure 2G. As shown in

A

Sapphire   Copper   VO₂

W_s L_s L_p S W_p L_v L_z W_v W_z W_m L_m

B

Port 5   Port 6
Port 4   V1   V5 V6   V2   Port 7
BBB-2   BBB-3
V7   V11
V8   V12
Port 3   BBB-1   V9 V10   BBB-4   Port 8
V3   V4
Port 2   Port 1
Y
O → X

G

					Units (mm)
Symbol	W	L	L_p	W_p	L_s
Size	36	40	10	12	6
Symbol	W_s	L_m	W_m	L_d	S
Size	0.5	3.5	0.5	0.5	4

C 2×2 antenna array

D 2×1 antenna array + filter

E 1×2 antenna array + filter

F 1×2 antenna array + filter

H

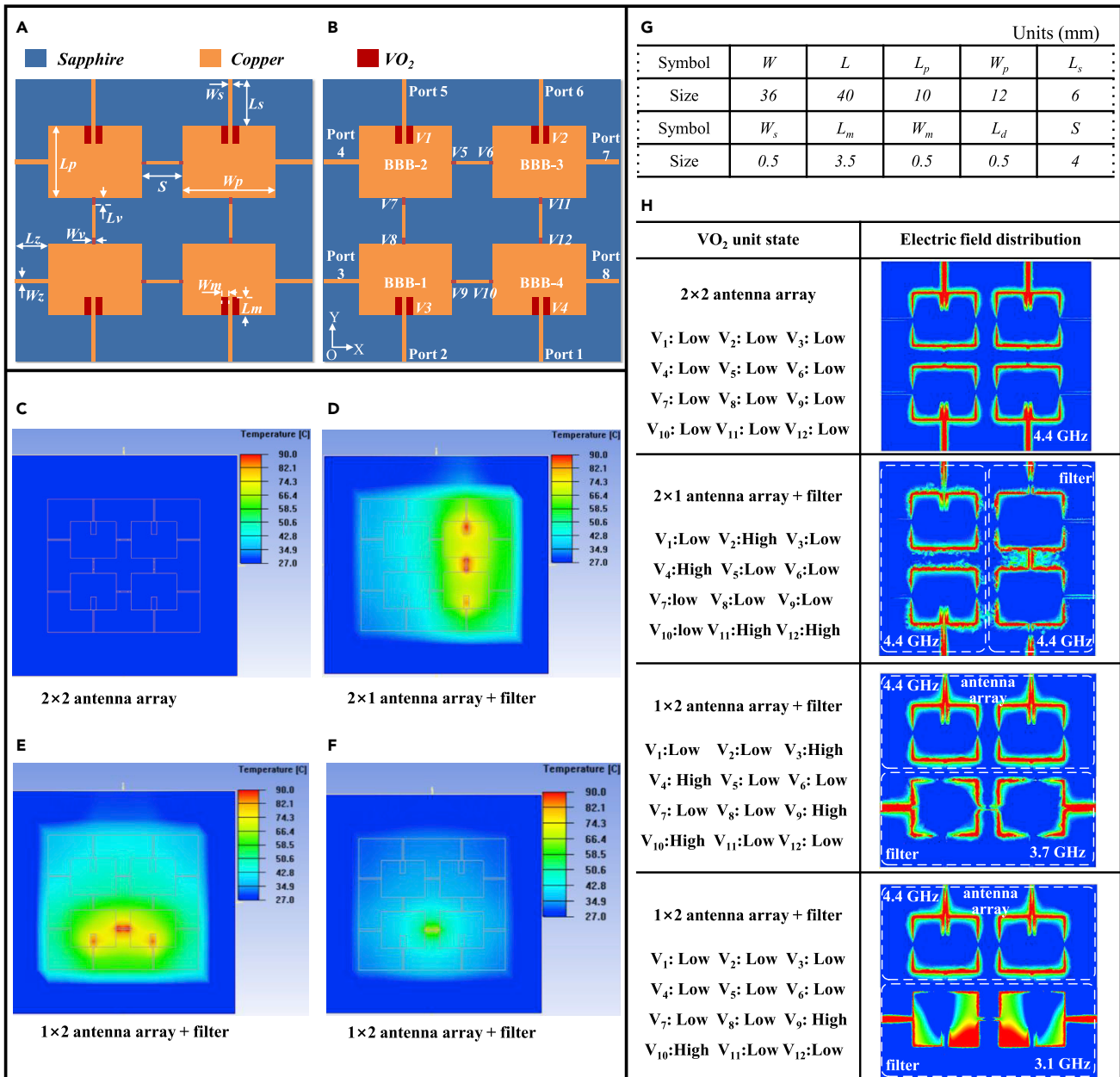| VO₂ unit state	Electric field distribution
2×2 antenna array V_1: Low V_2: Low V_3: Low V_4: Low V_5: Low V_6: Low V_7: Low V_8: Low V_9: Low V_{10}: Low V_{11}: Low V_{12}: Low	4.4 GHz
2×1 antenna array + filter V_1:Low V_2:High V_3:Low V_4:High V_5:Low V_6:Low V_7:low V_8:Low V_9:Low V_{10}:low V_{11}:High V_{12}:High	filter 4.4 GHz 4.4 GHz
1×2 antenna array + filter V_1:Low V_2:Low V_3:High V_4: High V_5: Low V_6: Low V_7: Low V_8: Low V_9: High V_{10}:High V_{11}:Low V_{12}: Low	4.4 GHz antenna array filter 3.7 GHz
1×2 antenna array + filter V_1: Low V_2: Low V_3: Low V_4: Low V_5: Low V_6: Low V_7: Low V_8: Low V_9: High V_{10}:High V_{11}:Low V_{12}:Low	4.4 GHz antenna array filter 3.1 GHz

Figure 2. Thermal control of reconfigurable devices

(A) The key dimensions of the array device.

(B) The configuration diagram of the 2 × 2 array device based on the BBBs. Label V1–V4 are multifunctional VO2 units for matching and perturbation. Label V5–V12 are VO2 switches.

(C–F) Different device functions are realized by temperature controlling the phase transition of VO2.

(G) Physical dimensions of the demonstrative functional reconfigurable.

(H)The combination of different working state VO₂ units and the corresponding RF electric field distribution.

Figure 2H, varying the phase of different VO₂ units will lead to different RF electric field distributions, resulting in different, reconfigurable microwave functions. VO₂ crystal lattice at monoclinic crystal state is represented by "Low" state. The VO₂ crystal lattice at tetragonal crystal state is represented by "High" state. Switching between various microwave configurations is realized by local control of the phase of eight VO₂ interconnect switches, labeled V_5 to V_{12}, and four VO₂ multifunctional matching & perturbation units, labeled V_1 to V_4.

Design method of the functionally reconfigurable microwave array device

As a reusable element, the design of the BBB should strike an appropriate balance among each reconfigurable microwave function as a reconfigurable narrowband antenna array and filter. The rectangular microstrip patch was chosen as the foundation of the BBB to fulfill the antenna and filter functions. Alternatively, for a demonstration of wideband microwave devices, a gap, coupled microstrip lines, or other non-resonant circuit structures could be used as the BBB. In our experiments, it was found that the amplitude of the VO$_2$ film conductivity swing could reach 1.2×10^3 S/m on single-crystal sapphire (Lee et al., 2018; Ha et al., 2013), which was chosen as the microwave dielectric substrate. Normally, a thicker substrate is helpful to antenna performance although unfavorable to filter performance (Li and Chen, 2018; Balanis, 2005). There are three alternative thickness of the sapphire substrate 254, 510, and 762 μm. To balance antenna gain and filter insertion loss, the substrate thickness was chosen to be 510 μm.

The microwave performance (resonance frequency, radiation pattern, and EM coupling) of the rectangular microstrip patch has been analyzed by using the theory of characteristic modes (Wu et al., 2021; Kumar and Khanna, 2020). The radiation performance of the patch antenna is mainly dependent on the dominant mode, TM$_{01}$. To realize the working frequency point 4.4 GHz of the antenna function, the length L_P of the rectangle patch is first calculated to 10 mm according to the antenna Equations (1) and (2). The 1st reconfigurable working frequency of the filter function is fixed in 4.4 GHz unselectively. Then, the width W_P of the rectangular patch is calculated to 12 mm according to the TM$_{10}$ resonator equation to ensure the 2nd reconfigurable working frequency point of the filter function is at 3.7 GHz (Drozd and Joines, 1998). The bandwidth of the patch antenna is not considered as a constraint in the design although it also is affected by W_P.

The reconfigurable filter with center frequency $f_{03} = 3.1$ GHz will be realized by using perturbation VO$_2$ unit that will be described in detail in the section D.

$$L_P = \frac{c}{2f\sqrt{\varepsilon_{eff}}} - 2\Delta L \qquad \text{(Equation 1)}$$

$$\Delta L = 0.412h \frac{(\varepsilon_{eff} + 0.3)\left(\frac{W_P}{h} + 0.264\right)}{(\varepsilon_{eff} - 0.258)\left(\frac{W_P}{h} + 0.8\right)} \qquad \text{(Equation 2)}$$

In which, ε_{eff} is the equivalent dielectric constant and h is the thickness of the sapphire substrate.

Once the basic sizes of the BBBs are fixed, the BBBs are combined which introduces additional trade-offs. To improve the reconfigurable performance of the microwave passive device, the FRMAD using a 2 × 2 array of BBBs was constructed as shown in Figure 2A. One of the crucial parameters in the design of the array device is the pitch S between two adjacent BBBs. The pitch greatly affects both the performance of the antenna array function and filter function and therefore should be determined with consideration of both microwave functions.

Generally, for antenna arrays, a larger value of pitch between BBBs will increase the antenna aperture and enhance the radiation gain. However, an excessive pitch will induce grating lobes in the radiation pattern. The upper limit of pitch is calculated by using Equation (3) in which N is the number of BBBs and λ is the wavelength. In contrast, reducing the pitch will lower the radiation gain. The gain curve of each antenna array function with respect to pitch S is depicted in Figure 3E.

$$d\text{max} < \frac{\lambda}{2}\left(\left(1 - \frac{1}{N}\right)\right) \qquad \text{(Equation 3)}$$

When the four BBBs are used as an antenna array, an appropriate distance S between the BBBs is able to enlarge the radiation aperture, which will improve the gain of the antenna array. However, the larger distance will reduce the capacitive coupling between the BBBs, which will affect the performance of the patch filter function. The inductive transmission microstrip line between the BBBs to offset the magnitude of this compromise to a certain extent was introduced (Dhwaj et al., 2018; Hong, 2011). The trade-offs between the two functions are shown in Figures 3E–3H. Based on the comprehensive evaluation above for the antenna array function and microstrip patch filter function, we set the pitch to $S = 4$ mm.
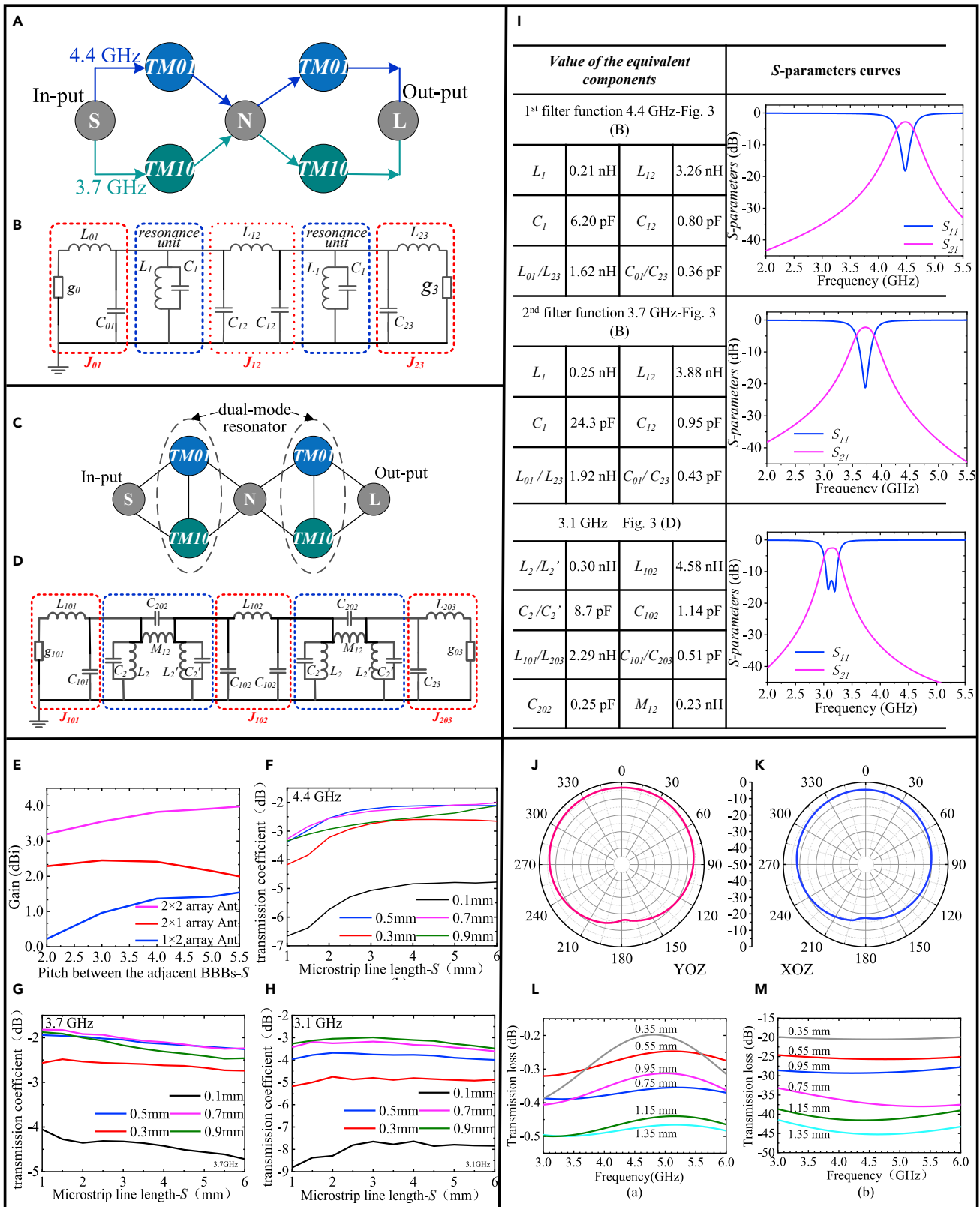
A

4.4 GHz

In-put

S — TM01 → N → TM01 → L — Out-put

S — TM10 → N → TM10 → L

3.7 GHz

B

L_{01} resonance unit L_{12} resonance unit L_{23}

g_0 L_1 C_1 C_{12} C_{12} L_1 C_1 g_3

C_{01} C_{23}

J_{01} J_{12} J_{23}

C

dual-mode resonator

In-put

S — TM01 — N — TM01 — L — Out-put

TM10 — TM10

D

L_{101} C_{202} L_{102} C_{202} L_{203}

g_{101} M_{12} M_{12} g_{03}

C_{101} C_2 L_2 L_2' C_2' C_{102} C_{102} C_2 L_2 L_2' C_2' C_{23}

J_{101} J_{102} J_{203}

I

Value of the equivalent components			S-parameters curves
1st filter function 4.4 GHz-Fig. 3 (B)			
L_1	0.21 nH	L_{12} 3.26 nH	
C_1	6.20 pF	C_{12} 0.80 pF	
L_{01}/L_{23}	1.62 nH	C_{01}/C_{23} 0.36 pF	
2nd filter function 3.7 GHz-Fig. 3 (B)			
L_1	0.25 nH	L_{12} 3.88 nH	
C_1	24.3 pF	C_{12} 0.95 pF	
L_{01}/L_{23}	1.92 nH	C_{01}/C_{23} 0.43 pF	
3.1 GHz—Fig. 3 (D)			
L_2/L_2'	0.30 nH	L_{102} 4.58 nH	
C_2/C_2'	8.7 pF	C_{102} 1.14 pF	
L_{101}/L_{203}	2.29 nH	C_{101}/C_{203} 0.51 pF	
C_{202}	0.25 pF	M_{12} 0.23 nH	

E

Gain (dBi) vs Pitch between the adjacent BBBs-S
- 2×2 array Ant
- 2×1 array Ant
- 1×2 array Ant

F

4.4 GHz — transmission coefficient (dB) vs Microstrip line length-S (mm)
- 0.1mm
- 0.5mm
- 0.3mm
- 0.7mm
- 0.9mm

G

3.7 GHz — transmission coefficient (dB) vs Microstrip line length-S (mm)
- 0.1mm
- 0.5mm
- 0.3mm
- 0.7mm
- 0.9mm

H

3.1 GHz — transmission coefficient (dB) vs Microstrip line length-S (mm)
- 0.1mm
- 0.5mm
- 0.3mm
- 0.7mm
- 0.9mm

J

YOZ

K

XOZ

L

Transmission loss (dB) vs Frequency(GHz)
- 0.35 mm
- 0.55 mm
- 0.95 mm
- 0.75 mm
- 1.15 mm
- 1.35 mm

(a)

M

Transmission loss (dB) vs Frequency (GHz)
- 0.35 mm
- 0.55 mm
- 0.95 mm
- 0.75 mm
- 1.15 mm
- 1.35 mm

(b)

Figure 3. Design method of the functionally reconfigurable microwave array device

(A) The topology of the 4.4 and 3.7 GHz band-pass filters.

(B) The equivalent circuit of the 4.4 and 3.7 GHz band-pass filter composed of two BBBs.

(C) The topology of the 3.1 GHz band-pass filters.

(D) The equivalent circuit of the 3.1 GHz band-pass filter composed of two BBBs with perturbation.

(E) The radiation gains of the antenna arrays vs. the pitch S between adjacent two BBBs.

(F–H) The transmission coefficient of the two BBBs vs. the pitch S with different line widths (0.1, 0.3, 0.5, 0.7, and 0.9 mm) at 4.4 GHz, at 3.7 GHz, and at 3.1 GHz.

(I) The value of equivalent components of the equivalent circuit and corresponding S-parameters.

(J–K) The radiation patterns of the 2 × 2 microstrip patch antenna array composed of BBBs (Plane YOZ & XOZ).

(L–M) The transmission characteristics of the microstrip line switch based on a VO$_2$ thin film (high conductivity state or low conductivity state) vs. the line length.

Because the planar configuration of the filter with center frequency of 4.4 and 3.7 GHz is symmetric to the vertical central line and horizontal central line of the patch, respectively, the coupling between the two modes TM$_{01}$/TM$_{10}$ can be neglected. The equivalent circuit of the double resonance units formed by adjacent BBB pairs is shown in Figures 3A and 3B. The energy transmission coefficients with respect to the connected BBBs via microstrip lines are shown in Figures 3F–3H.

On account of the low gain and efficiency caused in part by the sapphire substrate's high dielectric constant of 11.5, we preferred to widen the BBB pitch to increase the antenna array gain. Meanwhile, a 0.45 mm width microstrip line was used to connect adjacent BBBs to compensate for the compromised coupling coefficient and improve filtering performance measured by the *FBW* and insertion loss. In the following design, the VO$_2$ microstrip line switches are used to control the binary connection (connected for filter functions, disconnected for antenna array functions) between adjacent BBBs.

Once the design of the BBB array is fixed, the next step is to design the impedance matching circuit to connect each BBB to a 50 Ω adapter. As the BBB operating band is narrow, a quarter-wave impedance transformer was chosen to use, which is compact and effective for impedance matching in this application (Dong et al., 2020). The impedances at the access points in the center of the long and short sides of the BBB are 140 and 130 Ω, respectively. The corresponding line widths of the quarter-wave transformers are 0.4 and 0.38 mm, respectively. On account of edge effects, the quarter-wave transformers alone are unable to provide adequate feedlines for the antenna function. To enhance matching performance, an adjustable VO$_2$ trench is etched into the long side of the BBBs. The radiation pattern of the 2 × 2 microstrip patch antenna array can be calculated by feeding the four input ports as shown in Figures 3J and 3K.

Connections to the BBBs to configure the FRMAD as either an antenna array or a microstrip patch filter are controlled by VO$_2$ microstrip line switches. When the BBB is used in the antenna configuration, due to the edge effects of electromagnetic field, the quarter-wave transformer alone cannot enhance the return loss to an acceptable level alone. Typically, a rectangular trench will be etched onto the microstrip patch to improve the impedance matching (Jaiswal et al., 2019). In this article, rectangular multifunctional VO$_2$ film segments were used to act in place of a trench etched into the microstrip patch to trim the impedance match. In addition, the multifunctional VO$_2$ film trench also acts as a perturbation unit for the filter function. When the BBB is configured to a microstrip patch filter, a perturbation unit is activated on the BBB to adjust the characteristic mode of the BBB. Consequently, the performance of the filter can be reconfigured by adjusting the perturbation unit.

In this design, the impedance matching VO$_2$ trenches mentioned above also act as adjustable perturbation units to reconfigure the performance of the microwave filter function (Zhou et al., 2017). As the 3rd filter function has 3.1 GHz center frequency point, which is neither independent TM$_{01}$ or TM$_{10}$ resonance mode, the coupling coefficient between the odd mode and even mode by using perturbation should be enhanced (Gorur, 2004). Being different from the 1st reconfigurable filter function (4.4 GHz) and 2nd reconfigurable filter function (3.7 GHz), the equivalent circuit of the 3rd reconfigurable filter function will add the extra circuit to equivalent the mutual coupling between TM$_{01}$ and TM$_{10}$ mode as shown in Figures 3C and 3D).

The size of the multifunctional VO$_2$ film unit is L_m = 3.5 mm, W_m = 0.5 mm, determined by a comprehensive consideration of the matching performance and the perturbation influence. Then, the value of the
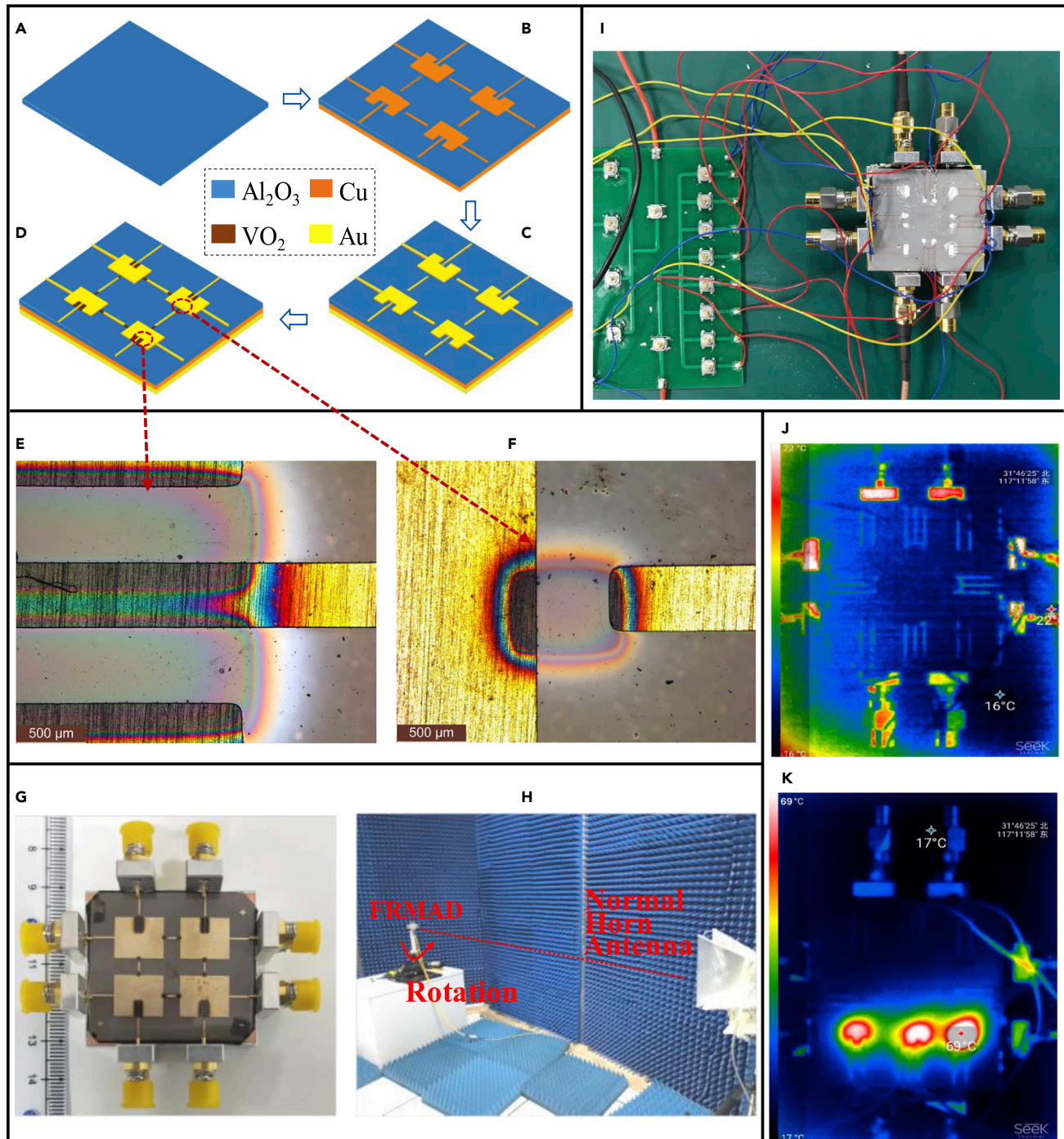
Figure 4. The fabrication process flow and the experimental test

(A) The single crystal phase sapphire used as the substrate.

(B) E-beam evaporation of a 1.5 µm Cu thin film on both sides of the sapphire substrate. The top Cu layer is patterned with a shadow mask during evaporation.

(C) A 0.3 µm Au thin film is deposited by E-beam evaporation to cover the top of the Cu thin film on both sides of the sapphire substrate with a mask during evaporation.

(D) A 0.6 µm VO2 thin film is sputtered locally onto the top side of the sapphire substrate with a shadow mask during sputtering.

(E) A representative optical photograph of the matching & perturbation multifunctional VO2 unit V1 under a microscope.

(F) A representative optical photograph of the VO2 microstrip line switch V8 under a microscope.

Figure 4. *Continued*

(G) The assembled functionally reconfigurable array device.

(H) The apparatus for far field testing of the antenna array.

(I) The plan view of the device with EPS and external current control panel for filter functions testing.

(J) The view of the plane thermal imaging with no directional heating.

(K) The view of the plane thermal imaging with directional heating of V_2, V_4, V_{11}, and V_{12} for the 4.4 GHz filter function.

equivalent circuit in Figures 3B and 3D is obtained and the corresponding *S*-parameters of the microwave filter configuration are simulated in Figure 3I.

The BBBs used in the antenna array and microstrip patch filter functions are accessed through RF current switches. Compared to P-I-N switches, the VO$_2$ film microstrip line switches have on-off functionality in the widely different conductivites of the available VO$_2$ phases. The VO$_2$ film RF switch can be conformal to the Cu microstrip line through E-beam deposition, which reduces the parasitic electromagnetic effects. Meanwhile, the risk of signal crosstalk could be reduced by means of temperature-control. As shown in Figure 3B, V_5, V_6, V_7, V_8, V_9, V_{10}, V_{11}, and V_{12} are VO$_2$ thin film microstrip line switches. The RF current flow can be redistributed by altering the switch state combinations.

Serving as RF switches, the core performance metrics of the VO$_2$ line switches are the insertion loss in the on-state and isolation in the off-state. The shorter the VO$_2$ line switch is, the lower the insertion loss will be, which benefits gain and efficiency. The high conductivity state is the on state while the low conductivity state is the off state. The length of the VO$_2$ microstrip lines L_v also demand the consideration of trade-offs between insert loss (in the on state) and isolation (in the off state). The simulated transmission losses when the VO$_2$ is in the on- and off-states are shown in Figures 3L and 3M. More long VO$_2$ microstrip line is good for EM isolation ($\geq$20dB) while is disadvantage to the insertion loss ($\leq$0.3dB@4.4 GHz). The length of the VO$_2$ microstrip line L_v was set to 0.35 mm to maximize the joint performances of the microstrip patch filter and antenna array configurations. Compared to conventional PIN diode switches, the VO$_2$ microstrip line reduces parasitic effects and requires no DC bias.

The fabrication process and test environment

In this work, a single-crystal sapphire wafer was used as the substrate to achieve the desired VO$_2$ phase transition characteristics as shown in Figure 4A. The VO$_2$ thin film was deposited by direct-current magnetron sputtering with a high-purity vanadium target. The growth pressure, Ar/O$_2$ gas flow, DC power, and temperature were 11.46 mTorr, 60/40 sccm, 200 W, and 550°C–700°C, respectively.

In consideration of compatibility with standard microwave integrated circuit processing, Cu was used as the primary conduction material, deposited by electron-beam (E-beam) evaporation. Shown in Figure 4B, the back side of the sapphire substrate was completely covered by a Cu layer with a thickness of 1.5 μm to act as the electrical ground. On the front side, a Cu layer was patterned to form the rigid circuit of the functionally reconfigurable device. To achieve a high-quality electrical connection between the SMA connectors and the microstrip transmission lines, a gold (Au) thin film with a thickness of 0.3 μm was deposited by E-beam evaporation to fully cover the surface of the Cu layer on both sides of the device as shown in Figure 4C. VO$_2$ thin film units, each with a thickness of ~0.6 μm were then sputtered locally onto the sapphire substrate as shown in Figure 4D. A shadow mask was designed and used to cover the top side of the device during sputtering.

An optical image of the fabricated FRMAD is shown in Figure 4G with all input and output microstrip terminals connected to SMA connectors. A representative multifunctional VO$_2$ matching & perturbation unit is shown in Figures 4E and 4A representative VO$_2$ interconnect switch is shown in Figure 4F, both as observed under an optical microscope. Using a shadow mask to pattern the VO$_2$ thin film during sputtering deposition unfavorably enlarged the boundary of the VO$_2$ film so that the actual widths of the films are larger than the design value. This process deviation takes blame for the minor discrepancy between the designed and the measured microwave electrical performance. Patterning the VO$_2$ thin film with photoresist rather than using a shadow mask could improve process accuracy. Figure 4H shows the far field-testing scene of the antenna functions. It should be noted that for the antenna functions testing, there is no VO$_2$ film unit phase transition, so the additional heating cover is not required.

To locally control the phase of the VO$_2$ thin films units, a flat expanded polystyrene (EPS) substrate and heat-conducting silicone (isolator) overlying the VO$_2$ units were used (note that antenna function doesn't
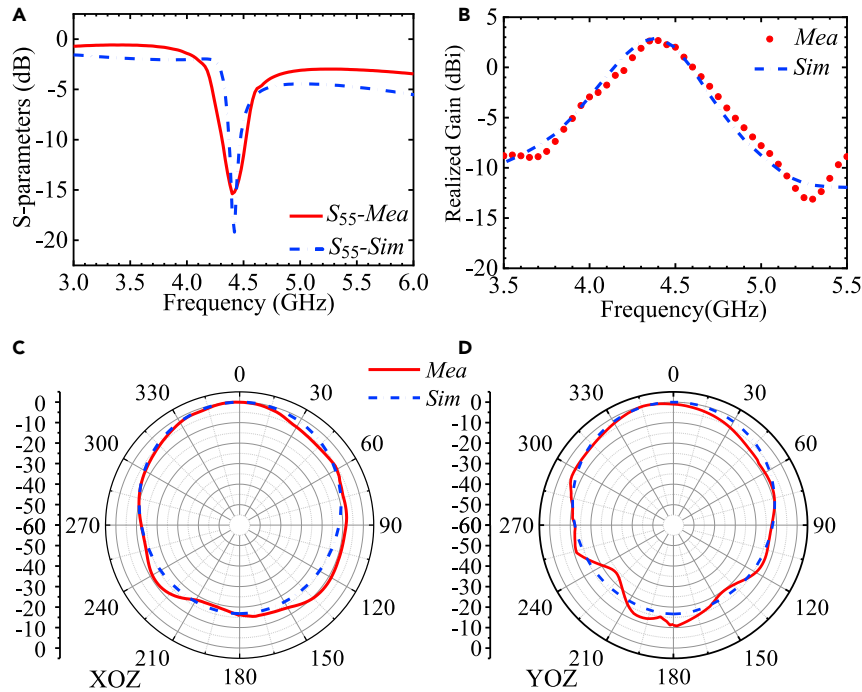
Figure 5. The performance of the 2 × 2 antenna array configuration
(A) The S_{11} of one of the identical four ports.
(B) The realized gain of the 2 × 2 antenna array configuration.
(C) The far field radiation pattern in the XOZ-plane.
(D) The YOZ-plane at 4.4 GHz.

require any phase transition of the VO_2). As shown in Figure 4I, there were 4 rectangular windows and 8 small rectangular windows on the EPS which correspond to the positions of the VO_2 units on the device. The heat-conducting silicone was packed into the windows and solidified.

The thin copper wires on the EPS were used as DC current controlled heating sources for each window/silicone pair. The temperature of the windows was monitored by infrared thermometry, ensuring that the phase transition of the VO_2 thin films would be triggered on demand. As the relative dielectric constant of expanded polystyrene is ~1.2, and the thin copper wire elements do not contact the device, the parasitic effects introduced by the heating setup are negligible. The temperature distribution of the plane is monitored by thermal imaging camera as shown in Figures 4J and 4K.

Result analysis

To test the functionality of the microwave filter configuration, the input and output ports were connected to two ports of a calibrated Keysight N5242A PNA-X. To test the functionality of the antenna array configuration, an RF signal was generated at one port of the Keysight N5242A and transmitted with a power of 10 dBm. Then, the RF signal was amplified to 30 dBm by a microwave power amplifier and radiated by a horn antenna. The functionally reconfigurable array device under testing, configured to act as receiving antenna, was placed 3 m away from the horn antenna and rotated with a motor over a 360° angle in order to vary the angle of incidence θ of the RF radiation on the receiving antenna in the XOZ-plane and the YOZ-planes. A comparison between the simulated and measured performance metrics of each EM function is shown in Figures 5, 6, and 7.

As shown in Figures 5A–5D, in the first configuration, as a 2 × 2 antenna array, the realized gain of the antenna was measured at over 2.85 dBi. Since the return loss curves of the four ports show good consistency, one of them was taken, S_{55}, for general demonstration and to represent the group. The measured S_{55} was lower than −14 dB at 4.4 GHz. Defining the plane seen from a top view as in Figure 2A as the XOY-plane, at 4.4 GHz, the 3-dB lobe width was greater than 58° and 60° on the YOZ-plane and XOZ-plane, respectively.
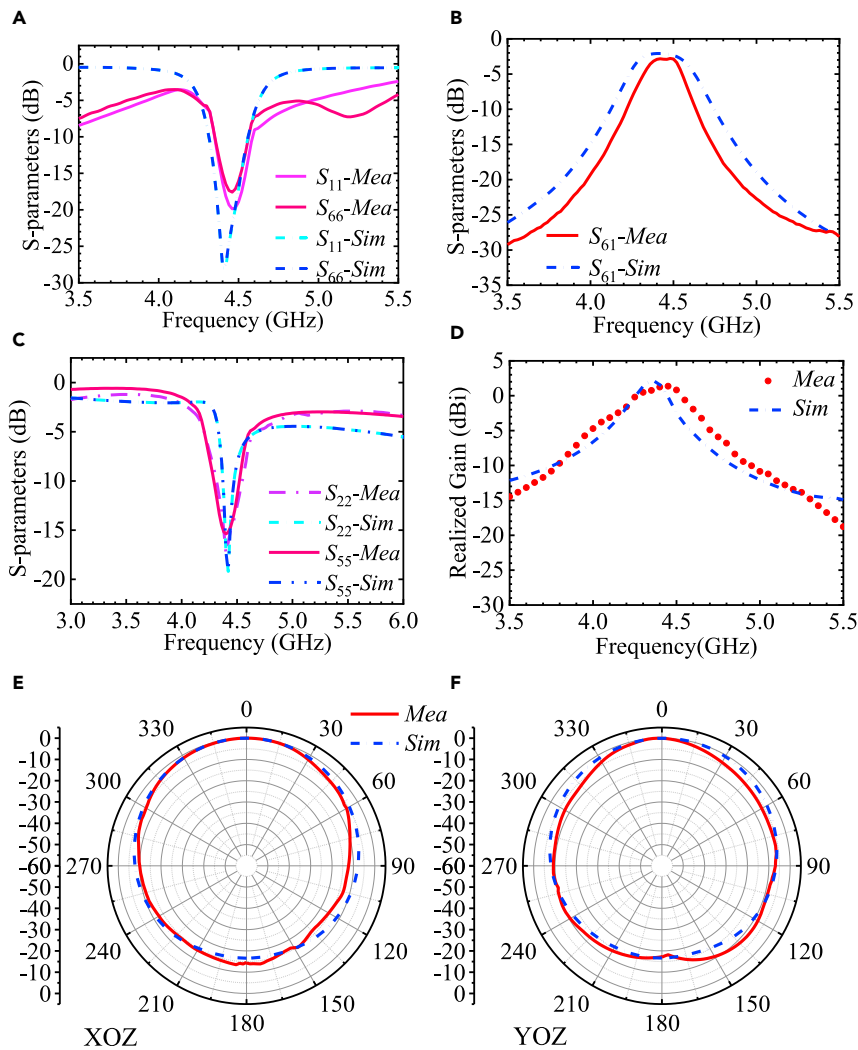
Figure 6. The performance of the 2 × 1 antenna array function and the longitudinal double cascade microstrip patch filter function

(A) The return loss of the input/output port of the filter.

(B) The transmission loss of the microwave pass-band filter.

(C) The loss of the two feed ports of the antenna array.

(D) The realized gain of the 2 × 1 antenna array configuration.

(E) The far field radiation pattern in the XOZ-plane.

(F) The YOZ-plane of the 2 × 1 antenna array configuration at 4.4 GHz.

In the second configuration, as a filter, BBB-1 and BBB-2 are used to assemble a 2 × 1 antenna array fed at ports 2 and 5. Meanwhile, BBB-3 and BBB-4 are connected along the Y axis in series by the VO$_2$ line switches V_{11} and V_{12}, input at port 1 and output at port 6. As shown in Figures 6A and 6B, the center frequency is 4.4 GHz with a bandwidth of 310 MHz and return loss greater than 11 dB in the bandwidth. The insertion loss is smaller than 2.2 dB and the stopband suppression is more than 15 dB at 500 MHz away from the center frequency point. The basic performance metrics of the 2 × 1 microstrip patch antenna array are shown in Figures 6C and 6D. The return loss is more than 15 dB at 4.4 GHz and the realized gain was 2.8 dBi. The radiation patterns of the patch microstrip antenna array in the XOZ-plane and the YOZ-plane are shown in Figures 6E and 6F. As the two BBBs are arranged along the Y axis, the 3-dB beam width is about 56° in the YOZ-plane and 92° in the XOZ-plane.

In the third configuration, BBB-2 and BBB-3 are used to assemble a 1 × 2 antenna array fed at ports 5 and 6. Meanwhile, BBB-1 and BBB-4 are connected along the X axis in series by VO$_2$ line switches V_9 and V_{10}, input
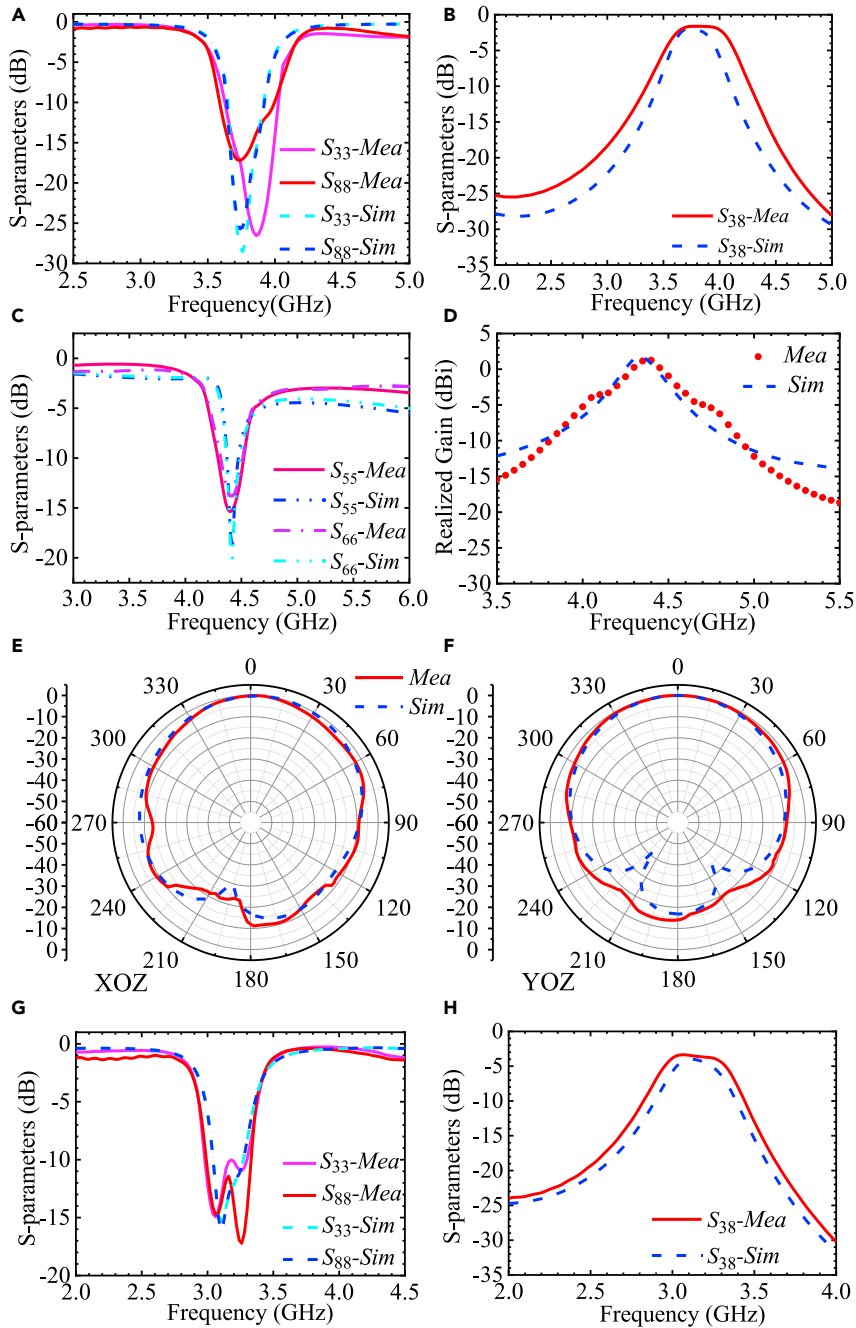
Figure 7. The performance of the 1 × 2 antenna array function and the transverse double cascade microstrip patch filter function

(A) The return loss of the input/output port of the filter when the VO_2 units V_3 and V_4 are in the high conductivity state.

(B) The transmission loss of the microwave pass-band filter when the VO_2 units V_3 and V_4 are in the high conductivity state.

(C) The loss at two of the feeding ports of the antenna array.

(D) The realized gain of the 1 × 2 antenna array function.

(E) The far field radiation pattern in the XOZ-plane.

(F) The YOZ-plane of the 2 × 1 antenna array configuration at 4.4 GHz.

(G) The return loss of the input and output ports of the filter when the VO2 units V3 and V4 are in the low conductivity state.

(H) The transmission loss of the microwave pass-band filter when the VO_2 units V_3 and V_4 are in the low conductivity state.

Table 1. The comparison of the performance with some published literature about reconfigurable filters

Ref.	Working Freq. (GHz)	Insert loss. (Max)	Relative Bandwidth	Other Functions
(Yang et al., 2020)	3.75–4	2.6dB	12%	NO
(Sumana et al., 2021)	1.60–2.27	4.2dB	6%	NO
(Chen and Chu, 2016)	0.98–1.22/1.63–1.95	4dB	5%	NO
(Maragheh et al., 2019)	1.8–2.5	3.2dB	4%	NO
(Song et al., 2019)	0.95–1.35	5.6dB	15%	NO
This work	3.1–4.4	2.8dB	8%	YES

at port 3 and output at port 8. With the multifunctional VO$_2$ units V_3 and V_4 having undergone a phase transition, as shown in Figures 7A and 7B, the center frequency is 3.7 GHz with a bandwidth of 390 MHz and the return loss is greater than 12 dB in the bandwidth. The insertion loss is smaller than 1.8 dB in the bandwidth and the passband suppression is more than 10 dB, 500 MHz away from the center frequency point. The performance metrics of the 1 × 2 microstrip patch antenna array are shown in Figures 7C and 7D. The return loss is more than 13 dB and the realized gain is 1.8 dBi at 4.4 GHz. The radiation patterns in the XOZ-plane and the YOZ-plane of the patch microstrip antenna array are shown in Figures 7E and 7F. As the two BBBs are arranged along the X axis, the 3-dB beam width is about 98° in the YOZ-plane and 62° in the XOZ-plane.

In the fourth configuration, the input and output ports are identical to those in the third configuration except that the phase of the multifunctional VO2 units V3 and V4 differ. In this configuration, V3 and V4 are in the low conductivity state, inducing the perturbation effect on the performance of the microstrip patch filter as shown in Figures 7G and 7H. The center frequency is 3.1 GHz with a bandwidth of 500 MHz. The return loss is more than 10 dB in the bandwidth. The insertion loss is smaller than 3.0 dB in the bandwidth and the stopband suppression is more than 15 dB 500 MHz away from the center frequency. The basic performance of the 1 × 2 microstrip patch antenna array remains like that of the third operating mode. The manufacturing process has a great influence on the result of our final experiment. Performance can be optimized by improving the conductance of VO2 of phase transition. In order to verify the repeatability of the design and fabrication method, other two samples with the same design were fabricated and measured, and the performance is compared and summarized in Section 3 in the supplemental information.

It has been shown that the performance metrics of each EM function meet basic requirements, meaning that the intended independently operating functions are able to be realized through the same device by adjusting the phase state of the VO$_2$ thin film units without reconstructing the device's physical structure. Small discrepancies between the simulated results and the measured data were observed, and can be attributed to the manual soldering of the SMA connectors and the unexpected shape and thickness variations of the VO$_2$ thin film units caused by imperfect masking during the manufacturing of these units. The performance of the FRMAD is compared with the published literature in Tables 1 and 2. It can be seen that the main properties of the FRMAD are not declined obviously.

System-level applications

An innovative configuration of the front-end circuit is described as shown in Figure 8. Due to the functionally reconfiguration of the FRMAD, the microwave link can be recombined to suitable for multipurpose

Table 2. The comparison of the performance with some published literature about reconfigurable antennas

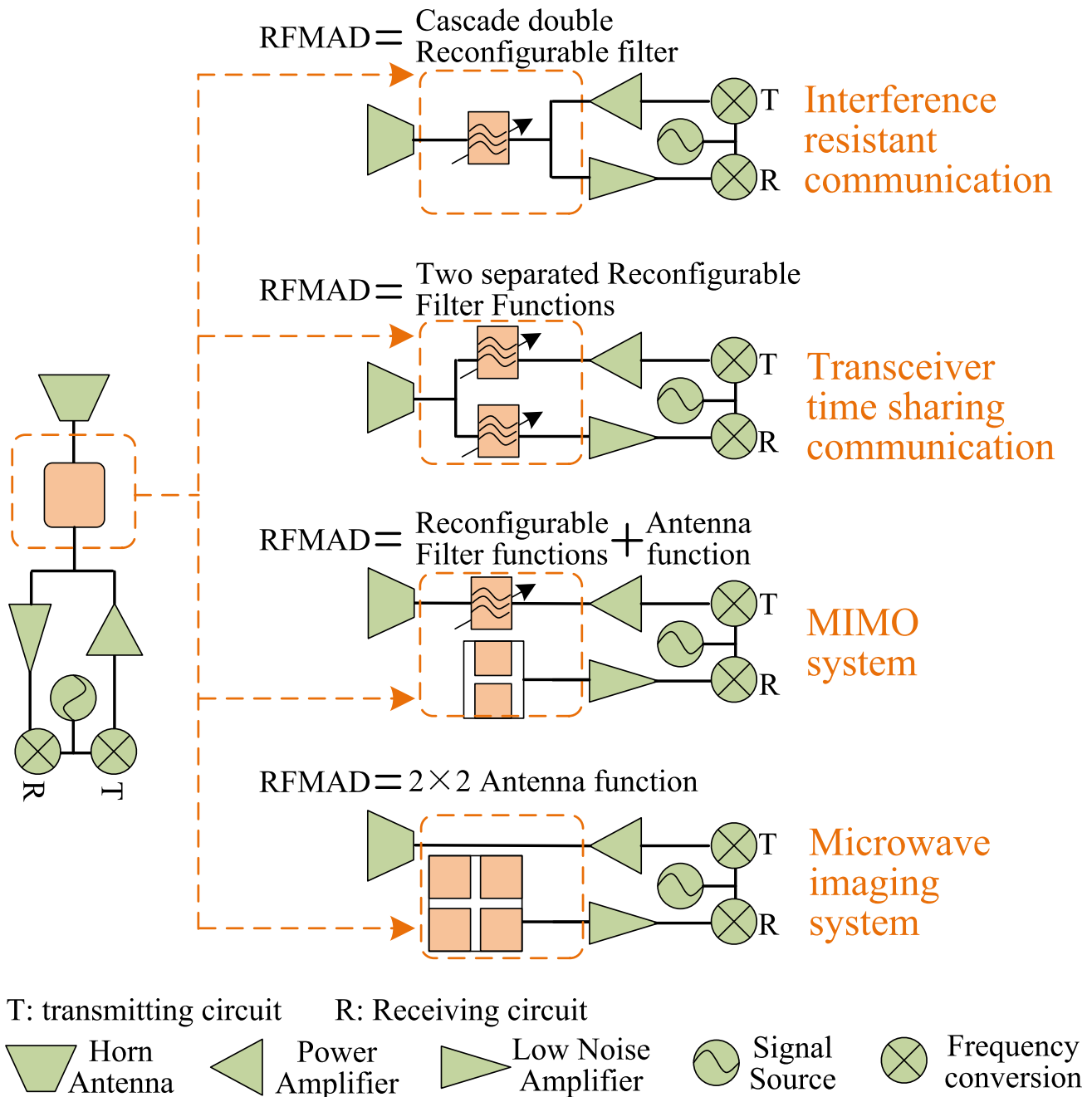| Ref.	Working Freq. (GHz)	Peak Gain	HPBW	Other Functions
(Anantha et al., 2017)	4.65–4.96	6.63dBi	92°/85°	NO
(Li et al., 2020)	4.9–5.55	7dBi	90°/60°	NO
(Prakash et al., 2021)	2.45	4dBi	110°/65°	NO
(Zainarry et al., 2018)	2.15–2.38	8.5dBi	50°/42°	NO
(Boukarkar et al., 2018)	2.35–3.43	4.3dBi	70°/60°	NO
This work	4.31–4.52	2.85dBi	58°/60°	YES

Figure 8. The potential transformative applications of the FRMAD in an RF front-end T/R circuit
The microwave-link can be reconstructed enabled by the reconcilable functions of the FRMAD.

system. For interference-resistant communication, the FRMAD can be reconfigured as a cascade band-pass filter, which has a more selective Tx and Rx frequency spectrum. For a transceiver time sharing circuit with both uplink and downlink capability, the FRMAD can be divided into two band-pass filters with different center operating frequency points. For a MIMO application, the FRMAD can be reconfigured partly as a band-pass filter used in Tx access and partly as a 2 × 1 antenna used in Rx access. The corresponding frequency spectrum shows that the Tx access has filtered the undesired frequencies and the Rx access has the expected reception pattern. For a microwave imaging system, the FRMAD could act as a 2 × 2 antenna array with Rx access, which could scan the beam more accurate.

It is true that the proposed reconfigurable microwave links based on the FRMAD can be realized by separate microwave devices, the main advantages of the FRMAD are summarized as follows:

1. Implementing FRMADs can reduce the number and variety of microwave devices purchased and used by systems designers as the same FRMAD are reusable across varying systems. The FRMAD can be used as two or more devices such as an antenna and filter as shown in Figure 8. For example, one FRMAD can be configured to serve in four types of microwave links in different applications. If the four types of the microwave links are realized by conventional separate devices, the types and number of the microwave devices will turn over a few times.

2. FRMADs make the operation and maintenance of microwave systems more efficient and convenient. As the FRMAD has multiple functions, a single type of FRMAD can replace a variety of malfunctioning devices in the field.

Conclusion and discussion

A thermal-controlled phase transition-enabled EM functionally reconfigurable 2 × 2 microwave array device is demonstrated by utilizing sputtered VO_2 thin film segments on a sapphire substrate. By thermal controlling the phase of the VO_2 microstrip line switches, which in turn modulates the switch conductivity, the rectangular patch BBBs can be flexibly reconfigured to function as an antenna array, frequency reconfigurable band-pass filter, or hybrid device with reconfigurable antenna and filter combined performance. Meanwhile, the feed line matching characteristics of the antenna, the bandpass of the filter can be optimized by adjusting the VO_2 multifunctional units. By carefully reconfiguring the EM functionality in time by varying the phase of the VO_2 units, the number of passive devices in a system including the present FRMAD can be reduced. Compared to the conventional understanding of reconfigurability, the concept of functional reconfigurability proposed in this paper demonstrates an expansion in generality to address the ever-present and increasingly urgent need to realize compact device footprints while concurrently improving the performance of high-frequency electronic devices and systems.

The reconfigurable performance can be enhanced with larger array scale and more VO_2 film. In order to implement the FRMAD in practical application, optimization on the performance of each microwave function is needed as well as the improvement of phase transition method such as using infrared light instead of heat.

Limitations of the study

The performance of the device is limited by the growth quality of VO_2 film. In this paper, the resistivity change ratio of VO_2 film grown by DC magnetron sputtering can reach the 3rd power, and according to the literature, it can reach the 5th power. The higher the change rate, the better the performance of the device.

STAR★METHODS

Detailed methods are provided in the online version of this paper and include the following:

- KEY RESOURCES TABLE
- RESOURCE AVAILABILITY
  - Lead contact
  - Materials availability
  - Data and code availability
- EXPERIMENTAL MODEL AND SUBJECT DETAILS
- METHOD DETAILS
  - Simulation of device
  - Fabrication of VO_2
  - Test of device
- QUANTIFICATION AND STATISTICAL ANALYSIS
- ADDITIONAL RESOURCES

SUPPLEMENTAL INFORMATION

Supplemental information can be found online at https://doi.org/10.1016/j.isci.2022.105060.

AUTHOR CONTRIBUTIONS

All the authors have contributed greatly. Conceptualization: Lei Sang and Wen Huang; Design: Lei Sang, Wen Huang, Zhikun Zhou, Ji Xu. Xing Li, and Wei He; Writing: Zhikun Zhou and Ji Xu.; Editing: Zhikun Zhou and Ji Xu; Simulation, Calculation, and experiment: Lei Sang, Zhikun Zhou, and Ji Xu. All authors discussed the results and commented on the manuscript.

DECLARATION OF INTERESTS

The authors declare no competing interests.

REFERENCES

Anantha, B., Merugu, L., and Somasekhar Rao, P. (2017). A novel single feed frequency and polarization reconfigurable microstrip patch antenna. AEU - Int. J. Electron. Commun. 72, 8–16. https://doi.org/10.1016/j.aeue.2016.11.012.

Balanis, C.A. (2005). Antenna Theory: Analysis and Design, 3rd (Wiley), pp. 826–828. Harper & Row. https://doi.org/10.1109/MAP.1982.27654.

Boukarkar, A., Lin, X.Q., Jiang, Y., and Yang, X.F. (2018). A compact frequency-reconfigurable 36-states patch antenna for wireless applications. IEEE Antenn. Wireless Propag. Lett. 17, 1349–1353. https://doi.org/10.1109/LAWP.2018.2846224.

Cai, M., Jiao, Z., Nie, S., Wang, C., Zou, J., and Song, J. (2021). A multifunctional electronic skin based on patterned metal films for tactile sensing with a broad linear response range. Sci. Adv. 7, eabl8313. https://doi.org/10.1126/sciadv.abl8313.

Chen, Z.H., and Chu, Q.X. (2016). Dual-band reconfigurable bandpass filter with independently controlled passbands and constant absolute bandwidths. IEEE Microw. Wireless Compon. Lett. 26, 92–94. https://doi.org/10.1109/LMWC.2016.2517153.

Cheng, R., Wang, F., Yin, L., Wang, Z., Wen, Y., Shifa, T.A., and He, J. (2018). High-performance, multifunctional devices based on asymmetric van der Waals heterostructures. Nat. Electron. 1, 356–361. https://doi.org/10.1038/s41928-018-0086-0.

Dhwaj, K., Jiang, L.J., and Itoh, T. (2018). Dual-band filtering antenna with novel transmission zero characteristics. IEEE Antenn. Wireless Propag. Lett. 17, 2469–2473. https://doi.org/10.1109/LAWP.2018.2878417.

Dong, E., Song, Z., Zhang, Y., Ghaffari Mosanenzadeh, S., He, Q., Zhao, X., and Fang, N.X. (2020). Bioinspired metagel with broadband tunable impedance matching. Sci. Adv. 6, eabb3641. https://doi.org/10.1126/sciadv.abb3641.

Drozd, J.M., and Joines, W.T. (1998). Using the binomial transformer to approximate the Q distribution for maximally flat quarter-wavelength-coupled filters. IEEE Trans. Microw. Theor. Tech. 46, 1495–1500. https://doi.org/10.1109/22.721153.

Gorur, A. (2004). Realization of a dual-mode bandpass filter exhibiting either a Chebyshev or an elliptic characteristic by changing perturbation's size. IEEE Microw. Wireless Compon. Lett. 14, 118–120. https://doi.org/10.1109/LMWC.2004.824811.

Ha, S.D., Zhou, Y., Fisher, C.J., Ramanathan, S., and Treadway, J.P. (2013). Electrical switching dynamics and broadband microwave characteristics of VO2 radio frequency devices. J. Appl. Phys. 113, 184501. https://doi.org/10.1063/1.4803688.

Hong, J.S. (2011). Microstrip Filters for RF Microwave Applications, 216, 2nd ed (Wiley), pp. 147–149. Texas A&M University. https://doi.org/10.1109/MMW.2002.1028365.

Huang, W., Yang, Z., Kraman, M.D., Wang, Q., Ou, Z., Rojo, M.M., Yalamarthy, A.S., Chen, V., Lian, F., Ni, J.H., et al. (2020). Monolithic mtesla-level magnetic induction by self-rolled-up membrane technology. Sci. Adv. 6, 4508–4525. https://doi.org/10.1126/sciadv.aay4508.

Huang, W., Zhou, J., Froeter, P.J., Walsh, K., Liu, S., Kraman, M.D., Li, M., Michaels, J.A., Sievers, D.J., Gong, S., and Li, X. (2018). Three-dimensional radio-frequency transformers based on a self-rolled-up membrane platform. Nat. Electron. 1, 305–313. https://doi.org/10.1038/s41928-018-0073-5.

Jaiswal, A., Abegaonkar, M.P., and Koul, S.K. (2019). Highly efficient, wideband microstrip patch antenna with recessed ground at 60 GHz. IEEE Trans. Antenn. Propag. 67, 2280–2288. https://doi.org/10.1109/TAP.2019.2894319.

Kumar, N., and Khanna, R. (2020). A compact multi-band multi-input multi-output antenna for 4G/5G and IoT devices using theory of characteristic modes. Int. J. RF Microw. Computer-Aided Eng. 30, e22012. https://doi.org/10.1002/mmce.22012.

Lee, D., Chung, B., Shi, Y., Kim, G.Y., Campbell, N., Xue, F., Song, K., Choi, S.Y., Podkaminer, J.P., Kim, T.H., et al. (2018). Isostructural metal-insulator transition in VO2. Science 362, 1037–1040. https://doi.org/10.1126/science.aam9189.

Li, H., Xiao, X., Wu, X., Ye, L., and Ji, G. (2021). scLINE: a multi-network integration framework based on network embedding for representation of single-cell RNA-seq data. J. Biomed. Inf. 122, 103899. https://doi.org/10.1016/j.jbi.2021.103899.

Li, M., Zhang, Z., and Tang, M.-C. (2020). A compact, low-profile, wideband, electrically controlled, tri-polarization-reconfigurable antenna with quadruple gap-coupled patches. IEEE Trans. Antenn. Propag. 68, 6395–6400. https://doi.org/10.1109/TAP.2020.2970073.

Li, T., and Chen, Z.N. (2018). Wideband substrate-integrated waveguide-fed endfire metasurface antenna array. IEEE Trans. Antenn. Propag. 66, 7032–7040. https://doi.org/10.1109/TAP.2018.2871716.

Luo, X., Yang, Z., Kraman, M., Sang, L., Zhang, Y., Li, X., and Huang, W. (2021). Physical modeling of monolithic self-rolled-up microtube interdigital capacitors. IEEE Trans. Compon. Packaging Manuf. Technol. 12, 359–367. https://doi.org/10.1109/TCPMT.2021.3128884.

Sedighi Maragheh, S., Dousti, M., Dolatshahi, M., and Ghalamkari, B. (2019). A dual-mode tunable bandpass filter for GSM UMTS WiFi and WiMAX standards applications. Int. J. Circ. Theor. Appl. *47*, 561–571. https://doi.org/10.1002/cta.2607.

Pan, C., Wang, C.Y., Liang, S.J., Wang, Y., Cao, T., Wang, P., Wang, C., Wang, S., Cheng, B., Gao, A., et al. (2020). Reconfigurable logic and neuromorphic circuits based on electrically tunable two-dimensional homojunctions. Nat. Electron. *3*, 383–390. https://doi.org/10.1038/s41928-020-0433-9.

Prakash, T., Chaudhary, R.K., and Gangwar, R.K. (2021). Pattern-reconfigurable antenna in azimuth plane using SP3T reconfigurable switching network. IET Microw., Antennas Propag. *15*, 62–68. https://doi.org/10.1049/mia2.12029.

Sang, L., Zhou, H., Yang, Z., Kraman, M.D., Zhao, H., Michaels, J.A., Sievers, D.J., Schutt-Aine, J.E., Li, X., and Huang, W. (2019). Monolithic radio frequency SiNx self-rolled-up nanomembrane interdigital capacitor modeling and fabrication. Nanotechnology *30*, 364001. https://doi.org/10.1088/1361-6528/ab244b.

Sang, L., Guo, X., Xu, J., Li, X., Kraman, M., Mei, Y., and Huang, W. (2020). Antenna-filter-splitter function reconfigurable microwave passive device based on VO2. IEEE Antenn. Wireless Propag. Lett. *19*, 1654–1658. https://doi.org/10.1109/LAWP.2020.3012192.

Sim, K., Rao, Z., Zou, Z., Ershad, F., Lei, J., Thukral, A., Chen, J., Huang, Q.A., Xiao, J., and Yu, C. (2019). Metal oxide semiconductor nanomembrane–based soft unnoticeable multifunctional electronics for wearable human-machine interfaces. Sci. Adv. *5*. https://doi.org/10.1126/sciadv.aav9653.

Song, K., Chen, W., Patience, S.R., Chen, Y., Iman, A.M., and Fan, Y. (2019). Compact wide-frequency tunable filter with switchable bandpass and bandstop frequency response. IEEE Access *7*, 47503–47508. https://doi.org/10.1109/ACCESS.2019.2908453.

Sui, J., and Wu, K.L. (2018). A capacitive loading method for turning a single-band Antenna into dual-band for wireless terminal applications. IEEE Antenn. Wireless Propag. Lett. *17*, 2474–2478. https://doi.org/10.1109/LAWP.2018.2878614.

Sumana, L., Sundarsingh, E.F., and Priyadharshini, S. (2021). Shape memory alloy-based frequency reconfigurable ultrawideband Antenna for cognitive radio systems. IEEE Trans. Compon. Packaging Manuf. Technol. *11*, 3–10. https://doi.org/10.1109/TCPMT.2020.3042738.

Wu, S.R., Lai, K.L., and Wang, C.M. (2018). Passive temperature control based on a phase change metasurface. Sci. Rep. *8*, 1–6. https://doi.org/10.1038/s41598-018 -26150-9.

Wu, Y., Lin, H., Xiong, J., Hou, J., Zhou, R., Deng, F., and Tang, R. (2021). A broadband metamaterial absorber design using characteristic modes analysis. J. Appl. Phys. *129*, 134902. https://doi.org/10.1063/5.0043054.

Yang, S., Li, W., Vaseem, M., and Shamim, A. (2020). Additively manufactured dual-mode reconfigurable filter employing VO2-based switches. IEEE Trans. Compon. Packaging Manuf. Technol. *10*, 1738–1744. https://doi.org/10.1109/TCPMT.2020. 3019067.

Zainarry, S.N.M., Nguyen-Trong, N., and Fumeaux, C. (2018). A frequency- and pattern-reconfigurable two-element array antenna. IEEE Antenn. Wireless Propag. Lett. *17*, 617–620. https://doi.org/10.1109/LAWP.2018.2806355.

Zhang, H.T., Park, T.J., Islam, A.N.M.N., Tran, D.S.J., Manna, S., Wang, Q., Mondal, S., Yu, H., Banik, S., Cheng, S., et al. (2022). Reconfigurable perovskite nickelate electronics for artificial intelligence. Science *375*, 533–539. https://doi.org/10.1126/science. abj7943.

Zhou, L.H., Chen, J.X., and Xue, Q. (2017). Design of compact coaxial-like bandpass filters using dielectric-loaded strip resonator. IEEE Trans. Compon. Packaging Manuf. Technol. *8*, 456–464. https://doi.org/10.1109/TCPMT.2017. 2786293.

STAR★METHODS

KEY RESOURCES TABLE

REAGENT or RESOURCE	SOURCE	IDENTIFIER
Software and algorithms		
ANSYS	ANSYS. Co., LTD	https://www.ansys.com/zh-cn
Other		
Vanadium	Nanjing Special Gas Plant Co. LTD	RRID:SCR_008218; http://www.njtq.cn/m/product/
Oxygen	Nanjing Special Gas Plant Co. LTD	RRID:SCR_008218; http://www.njtq.cn/m/product/
Argon Gas	Nanjing Special Gas Plant Co. LTD	RRID:SCR_008218; http://www.njtq.cn/m/product/

RESOURCE AVAILABILITY

Lead contact

Further information and requests for resources should be directed to and will be fulfilled by the lead contact, Wen Huang (huangw@hfut.edu.cn).

Materials availability

Devices generated in this study will be available from the Authors upon request.

Data and code availability

All data reported in this paper will be shared by the lead contact upon request. The current study did not generate any new Code. Any additional information required to reanalyze the data reported in this paper is available from the lead contact upon request.

EXPERIMENTAL MODEL AND SUBJECT DETAILS

The electrical performance of the device was simulated by High Frequency Structure Simulator, and VO_2 was fabricated by magnetron sputtering method.

METHOD DETAILS

Simulation of device

The reconfigurable array device was modeled in the commercial 3D electromagnetic field analysis software High Frequency Structure Simulator (HFSS) by Ansys. HFSS frequency domain solver is used in this paper. The simulation frequency is in the range of 2-3 GHz from the center frequency of antenna and filter. The simulation calculation step is 0.02 GHz. There are two sets of material parameters necessary to describe the properties of the VO_2 thin film corresponding to the phase state before the transition (conductivity: 950 S/m) and the phase state after the transition (conductivity: 1.1×10^6 S/m). The S parameter can be directly extracted according to the port number as shown in Figure 2B.

Fabrication of VO_2

Ar and O_2 are charged into the vacuum and gas discharge is produced under strong electric field, which produces high-energy ions and shoots toward vanadium target (Ar: O_2 = 90:10). The accelerated ion bombards the vanadium target, bombards the atoms of the vanadium target, and obtains the deposited material, which is deposited on the substrate and condensed into a VO_2 film.

Test of device

The reconfigurable array device was tested by vector network analyzer (for filter) and Microwave anechoic chamber (for antenna). The microwave anechoic chamber adopts the method of near-field testing. The

system consists of three parts: mechanical scanning frame with optical measurement subsystem, radio frequency subsystem and automatic control system. The RF subsystem is usually connected to a probe by a microwave receiver (such as a spectrum analyzer and a vector network analyzer), which moves on the plane in front of the antenna under computer control and collects the electric field strength.

There are two methods of gain testing: comparative and direct. In the comparison method, the reference antenna is the standard gain horn, and in the direct method, the reference antenna is the probe. We used the comparative method to measure the gain, which is to compare the far-field receiving level of the antenna under test with the receiving level of the standard antenna under the same conditions, and the difference between the two is the difference of its gain.

Filter was tested by using a vector network analyzer with the upper limit of the measurement frequency of 49.5 GHz (R&S (Rohde & Schwarz) ZNA 43–44). The measurement port model is ZV-Z229. The S parameter can be directly measured by vector network analyzer.

QUANTIFICATION AND STATISTICAL ANALYSIS

The simulation data is produced by ANSYS HFSS software. Figures shown in the main text were produced by Origin and Microsoft PowerPoint from the raw data.

ADDITIONAL RESOURCES

Any additional information about the simulation and data reported in this paper is available from the lead contact on request.